Topological magnonics in the two-dimensional van der Waals magnet CrI_3

Esteban Aguilera,[1,*] R. Jaeschke-Ubiergo,[1] N. Vidal-Silva,[2,3] Luis E. F. Foa Torres,[1] and A. S. Nunez[1,3]

[1]*Departamento de Física, FCFM, Universidad de Chile, 8370456 Santiago, Chile*

[2]*Departamento de Ciencias Físicas, Universidad de La Frontera, Casilla 54-D, 4811186 Temuco, Chile*

[3]*CEDENNA, Universidad de Santiago de Chile, Avda. Ecuador 3493, Santiago, Chile*

(Received 20 March 2020; accepted 15 June 2020; published 6 July 2020)

We report on the magnon spectrum of Kitaev-Heisenberg magnets and extract the parameters to model a two-dimensional CrI_3. Our minimal spin Hamiltonian includes a contribution stemming from a Heisenberg, isotropic exchange, and a contribution arising from a Kitaev interaction, anisotropic and frustrated exchange. Our calculations reveal a gap that opens at the K and K' points and the topological nature of the magnons which lead to the thermal Hall effect. Furthermore, we calculate the magnon spectrum of nanoribbons illustrating the corresponding edge states.

DOI: 10.1103/PhysRevB.102.024409

I. INTRODUCTION

The graphene revolution led the way into the world of two-dimensional materials [1], with properties that baffled the usual behavior found in their three-dimensional counterparts. The path was followed with enthusiasm by early practitioners and has fruitfully rewarded them with a plethora of 2D materials and van der Waals heterostructures [2] with groundbreaking properties. The list of discoveries grows steadily and includes a variety of semiconductors [3], superconductors [4,5], and ferroelectrics [6]. Spintronic devices [7] are also intensively targeted [8] as one of the most promising applications. In 2017, new forms of 2D materials were reported to display ferromagnetism, a state of matter elusive in the two-dimensional realm until then [9,10]. In particular, a van der Waals material, single-layer CrI_3, was reported to display ferromagnetism [9] under 45 K. To overcome 2D thermal fluctuations that would otherwise render its magnetization unstable [11], CrI_3 relies heavily upon several forms of anisotropy [12].

In this work, we report on the collective behavior of the magnetic degrees of freedom of two dimensional magnets such as CrI_3 in the form of magnons. Magnons are quantized low-energy excitations of the magnetization field [13]. Their control and manipulation might lead to novel applications in the field of magnon spintronics [14,15]. As we detail below, these excitations in CrI_3 seem to defy the standard wisdom in magnetism and display unusual behavior with potential applications in several areas such as quantum computing and spintronics.

The reason for these unusual properties is that CrI_3, as recently proposed [16,17], is described by a Kitaev's interaction. Since the material is essentially composed of an honeycomb lattice of edge sharing octahedra, it is natural to expect similarities with layered Na_2IrO_3 and α-$RuCl_3$ well known for its behavior dominated by a Kitaev Hamiltonian [18]. This interaction is an anisotropic form of frustrated exchange that, when acting alone, unleashes a formidable gallery of topologically protected magnetic excitations, such as anyons and Majorana excitations [19,20]. Like other systems that have been proposed as implementation of topological magnonics [21–24], the current proposal offers a way into controllable excitations with great potential in the context of magnonic devices.

II. MODEL

The magnetic degrees of freedom in the CrI_3 ferromagnet can be modeled using the Heisenberg-Kitaev model. Chromium sites form a magnetic honeycomb lattice, with magnetic moment $S = 3/2$. The Hamiltonian consists in the usual isotropic Heisenberg exchange, plus an anisotropic contribution that comes from Kitaev model. The magnetic Hamiltonian takes the form

$$H = -\sum_{\langle i,j\rangle}\left(J\mathbf{S}_i\cdot\mathbf{S}_j + KS_i^{\gamma}S_j^{\gamma}\right) - \sum_i A\left(S_i^z\right)^2. \tag{1}$$

Here the first summation runs over nearest neighbors, and we define $S_i^{\gamma} \equiv \mathbf{S}_i\cdot\hat{\boldsymbol{\gamma}}$, as the component of the magnetic moment in the $\hat{\gamma}$ direction. These directions depend on the link, so $\hat{\boldsymbol{\gamma}}$ should be understood in (1) as an abbreviation of $\hat{\boldsymbol{\gamma}}_{ij}$. J and K are the Heisenberg and Kitaev exchange constants, respectively. We also include an easy-axis anisotropy of magnitude A.

We are considering nearest neighbors in a honeycomb lattice, so we have three kinds of links on each unit cell. Figure 1 shows the links and the respective $\hat{\boldsymbol{\gamma}}_a$ directions. Note that each $\hat{\boldsymbol{\gamma}}_a$ points normal to the Cr_2I_2 plaquette that contains the link $\hat{\mathbf{l}}_a$. The explicit form of $\hat{\boldsymbol{\gamma}}_a$ vectors in the basis xyz is

$$\hat{\boldsymbol{\gamma}}_1 = \left(0, \frac{-\sqrt{2}}{\sqrt{3}}, \frac{1}{\sqrt{3}}\right), \tag{2a}$$

$$\hat{\boldsymbol{\gamma}}_2 = \left(\frac{1}{\sqrt{2}}, \frac{1}{\sqrt{6}}, \frac{1}{\sqrt{3}}\right), \tag{2b}$$

$$\hat{\boldsymbol{\gamma}}_3 = \hat{\boldsymbol{\gamma}}_1 \times \hat{\boldsymbol{\gamma}}_2. \tag{2c}$$

*Corresponding author: aguilera.marinovic@gmail.com

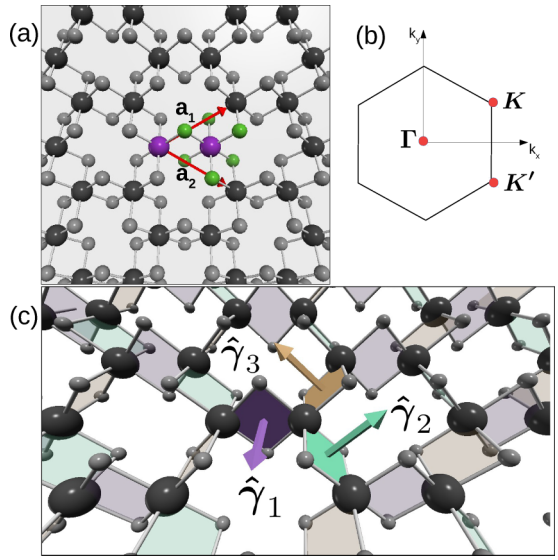

FIG. 1. (a) Top view of CrI_3 monolayer. The atoms in the unit cell are highlighted in color: big purple spheres represent chromium sites and small green spheres represent iodine sites. Lattices vectors $\mathbf{a_1} = a_0(\frac{\sqrt{3}}{2}, \frac{1}{2}, 0)$ and $\mathbf{a_2} = a_0(\frac{\sqrt{3}}{2}, -\frac{1}{2}, 0)$ were drawn with red arrows, a_0 is the lattice constant. (b) First Brillouin zone, with the special symmetry points $\mathbf{\Gamma}$, $\mathbf{K}$, and $\mathbf{K'}$.(c) A view of the CrI_3 monolayer in perspective, with the plaquettes Cr_2I_2 colored according to their normal vectors $\hat{\boldsymbol{\gamma}}_\mathbf{1}$, $\hat{\boldsymbol{\gamma}}_\mathbf{2}$, and $\hat{\boldsymbol{\gamma}}_\mathbf{3}$. Three plaquettes in the unit cell are highlighted, and normal vectors form an orthonormal basis.

Where it is important that $\{\hat{\boldsymbol{\gamma}}_a\}$ vectors form an orthonormal basis oriented as shown in Fig. 1. The orientation of this triad and the presence of the additional anisotropy make this model different from the one described in Refs. [25,26].

Both, the Heisenberg and Kitaev contributions to the overall exchange interaction, that can be put together using a single exchange matrix $\mathcal{J}_{ij}$ in the form $-\sum_{\langle i,j\rangle} \mathbf{S}_i \cdot \mathcal{J}_{ij} \cdot \mathbf{S}_j$. The matrix $\mathcal{J}_{ij}$ can take, depending on the link, one of three different forms $\mathcal{J}_1$, $\mathcal{J}_2$ or $\mathcal{J}_3$. The matrix $\mathcal{J}_a$ takes the form: $\mathcal{J}_a = J\mathbb{1} + K\gamma_a \otimes \gamma_a$. It is important to note that $\mathcal{J}_a$ remains invariant under the transformation $\hat{\boldsymbol{\gamma}}_a \to -\hat{\boldsymbol{\gamma}}_a$.

A. Magnons

We are interested in obtaining, from Hamiltonian (1), the Hamiltonian for magnons. This can be done by means of the Holstein-Primakoff transformation [27]:

$$S^{(x)}_{i\mu} = \sqrt{\frac{S}{2}}(\psi^\dagger_{i\mu} + \psi_{i\mu}), \tag{3a}$$

$$S^{(y)}_{i\mu} = i\sqrt{\frac{S}{2}}(\psi^\dagger_{i\mu} - \psi_{i\mu}), \tag{3b}$$

$$S^{(z)}_{i\mu} = S - \psi^\dagger_{i\mu}\psi_{i\mu}, \tag{3c}$$

where $\mu \in \{A, B\}$ indexes the two lattices conforming the bipartite honeycomb array of Cr atoms.

When the transformation is replaced in the Hamiltonian and reduced to quadratic terms, we obtain a Hamiltonian in terms of $\mathbf{\Psi_k} = (\psi_{A\mathbf{k}}, \psi_{B\mathbf{k}}, \psi^\dagger_{A-\mathbf{k}}, \psi^\dagger_{B-\mathbf{k}})^t$, in the form $\mathcal{H} = \frac{1}{2}\sum_\mathbf{k} \mathbf{\Psi_k}^\dagger \mathbf{H_k} \mathbf{\Psi_k}$, where

$$\mathbf{H}_k = \begin{pmatrix} \varepsilon & \alpha_k & 0 & \beta_k \\ \alpha^*_k & \varepsilon & \beta_{-k} & 0 \\ 0 & \beta^*_{-k} & \varepsilon & \alpha_k \\ \beta^*_k & 0 & \alpha^*_k & \varepsilon \end{pmatrix}. \tag{4}$$

In the above expression, we have defined the variables

$$\varepsilon = S(3J + K + 2A), \tag{5a}$$

$$\alpha_k = \sum_a \alpha_a e^{i\mathbf{k}\cdot\boldsymbol{\delta}_a}, \tag{5b}$$

$$\beta_k = \sum_a \beta_a e^{i\mathbf{k}\cdot\boldsymbol{\delta}_a}, \tag{5c}$$

where $\boldsymbol{\delta}_a$ are vectors expressed in terms of lattice vectors as: $\boldsymbol{\delta}_1 = 0$, $\boldsymbol{\delta}_2 = \mathbf{a_1}$, and $\boldsymbol{\delta}_3 = \mathbf{a_2}$, and we have defined the following quantities:

$$\alpha_a = -S\big(\mathcal{J}^{xx}_a + \mathcal{J}^{yy}_a\big)/2, \tag{6a}$$

$$\beta_a = -S\big(\mathcal{J}^{xx}_a - \mathcal{J}^{yy}_a\big)/2 - iS\mathcal{J}^{xy}_a. \tag{6b}$$

B. Eigenenergies and eigenstates

The eigenenergies and eigenstates of Hamiltonian (4) can be directly obtained by means of a Bogoliubov transformation [28]. Defining the constants $\epsilon_0 = S(3J + K)$, $\mathcal{K} = KS/\epsilon_0$ and $\mathcal{A} = 2AS/\epsilon_0$, the eigenvalues are found to be

$$\epsilon^2_\pm(\mathbf{k}) = \frac{\epsilon_0^2}{9}\Big(f(\mathbf{k}) \pm \sqrt{g(\mathbf{k})}\Big), \tag{7}$$

where the functions $f = f_0 + f_\mathcal{A} + f_\mathcal{K}$ and $g = g_0 + g_\mathcal{A} + g_\mathcal{K}$ are defined in Appendix A, separating the contributions of the Kitaev and Anisotropy terms, in such a way $f_{\mathcal{A},\mathcal{K}}$ and $g_{\mathcal{A},\mathcal{K}}$ are zero when the anisotropy or Kitaev terms are neglected.

We plot the energy spectrum, across the first Brillouin zone in Fig. 2. The vanishing energy Goldstone mode at the $\mathbf{\Gamma}$ point is lifted to $\Delta_\mathbf{\Gamma}$ by the inclusion of the anisotropy term, A. We can see clearly that in the case of absence of the Kitaev contribution the spectrum is degenerate at the $\mathbf{K}$ and $\mathbf{K}'$ points. This degeneracy is lifted by the inclusion of the Kitaev term, leading to the opening of a gap of magnitude $\Delta_\mathbf{K}$.

In the vicinity of the $\mathbf{\Gamma}$ point, the low-energy band behaves as

$$\epsilon_-(\mathbf{k}) = 2AS + \epsilon_0 a_0^2\left(\frac{2 + 2\mathcal{A} - \mathcal{K}^2}{24(1+\mathcal{A})}\right)|\mathbf{k}|^2$$

and we identify the usual structure $\epsilon = \Delta_\mathbf{\Gamma} + \rho_\mathbf{\Gamma}\mathbf{k}^2$, where $\Delta_\mathbf{\Gamma} = 2AS$ and $\rho_\mathbf{\Gamma} = \epsilon_0 a_0^2(\frac{2+2\mathcal{A}-\mathcal{K}^2}{24(1+\mathcal{A})})$. $\Delta_\mathbf{\Gamma}$ correspond to the minimal energy necessary to create a magnon. It turns out to be a fundamental quantity and can be accessed experimentally. It lies between 1 and 9 meV [29] while *ab initio* calculations locate it in the range of 1 meV [30]. $\rho_\mathbf{\Gamma}$ is the effective low-energy spin stiffness. It is an estimate of how hard it is to introduce a smooth texture in the magnetization field.

The behavior of the top band at $\mathbf{\Gamma}$ point is

$$\epsilon_+(\mathbf{k}) = 2\epsilon_0 + \Delta_\mathbf{\Gamma} - \rho'_\mathbf{\Gamma}|\mathbf{k}|^2,$$

which shows that the bandwidth, defined as the energy difference $\epsilon_+ - \epsilon_-$ at $\mathbf{\Gamma}$ point, is given by $2\epsilon_0 = 2S(3J + K)$.

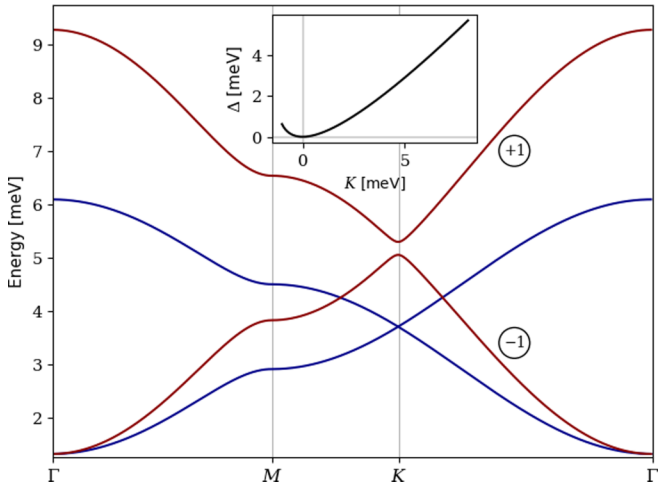

FIG. 2. Energy spectrum of magnons within the first Brillouin zone. The blue line corresponds to the case $J = 0.53$ meV, $A = 0.44$ meV, and $K = 0$. It can be see that there is no gap at the **K** point. There is a gap at the Γ point that arises from the anisotropy contribution [12]. On the other hand, the inclusion of the Kitaev interaction, $K = 2J$ displayed in the red line, displays a gap opening at the **K** point revealing a nontrivial topology. The circles next to each bands correspond to the associated Chern numbers. These are calculated according to [21]. The **K**-point gap is calculated as a function of the Kitaev interaction strength in the inset.

The effective Hamiltonian in the vicinity of **K** and **K**′ is given by

$$\mathbf{H}_{\mathbf{K}^{(\prime)}}(\mathbf{q}) = \begin{pmatrix} \mathbf{T}_{\mathbf{q}} & \mathbf{U}^{(\prime)} \\ \mathbf{U}^{(\prime)\dagger} & \mathbf{T}_{\mathbf{q}} \end{pmatrix}, \tag{8}$$

where

$$\mathbf{T}_{\mathbf{q}} = \epsilon_0 \begin{pmatrix} 1+\mathcal{A} & i\kappa \\ -i\kappa^* & 1+\mathcal{A} \end{pmatrix}$$

and **U** is written with the aid of the spin-1/2 ladder operator as $\mathbf{U} = K\sigma^-$. The matrix $\mathbf{U}'$ at the other valley corresponds to $\mathbf{U}' = \mathbf{U}^\dagger$. Here we have defined $\mathbf{q} = \mathbf{k} - \mathbf{K}^{(\prime)}$ and $\kappa = a_0(q_x + iq_y)/(2\sqrt{3})$, with a_0 being the lattice constant. In the definition of **U**, we have dropped linear terms in **q** under the assumption of the small Kitaev parameter. Energies around **K** and **K**′ take the form

$$\epsilon^{\pm}(\mathbf{q}) = E_{\mathbf{K}} \pm \frac{\Delta_{\mathbf{K}}}{2} \pm \rho^{\pm}_{\mathbf{K}}|\mathbf{q}|^2$$

with $E_{\mathbf{K}} = \frac{\epsilon_0}{2}(1 + \mathcal{A} + \sqrt{(1+\mathcal{A})^2 - \mathcal{K}^2})$ and $\Delta_{\mathbf{K}} = \epsilon_0(1 + \mathcal{A} - \sqrt{(1+\mathcal{A})^2 - \mathcal{K}^2})$. All those features are in agreement with Ref. [30], which can be used to adjust our parameters. We find $J \sim 0.53$ meV, $K \sim 4.07$ meV, and $A \sim 0.44$ meV, in same range as Ref. [16].

C. Chern numbers

The band structure found by this method reveals a nontrivial topological structure, which is present both in the full model (4) and even in the minimal model of equation (8). This is in agreement with the results of Ref. [26] for a similar geometrical construction. The Chern numbers of the bands, calculated according to Ref. [21], are displayed in next to each band. The Chern number of the jth energy band is given by

$$C_j = i\frac{\epsilon_{\mu\nu}}{2\pi}\int_{\mathrm{BZ}} d^2k Tr\big[(1-P_j)\big(\partial_{k_\mu}P_j\big)\big(\partial_{k_\nu}P_j\big)\big]. \tag{9}$$

The integrand of the Chern number is called the Berry curvature, $\mathbf{\Omega}^j_{\mathbf{k}}$, and P_j are the projection operators, which are defined as

$$P_j = T_{\boldsymbol{k}}\Gamma_j\sigma_3 T^\dagger_{\boldsymbol{k}}\sigma_3, \tag{10}$$

where we have that $T_{\boldsymbol{k}}$ is the transformation matrix obtained by Colpa's algorithm [28], σ_3 is the paraunitary matrix, and Γ_j is a $(2N, 2N)$ matrix where every element is 0 except for the jth diagonal component, where it has a value of 1.

It is also important to note that the value of the Chern numbers does not revert its sign when K passes from a positive value to a negative one. Therefore an interface between samples with different signs of K would not host topological states as there is no change in the Chern number between the regions. This is because a chirality is already fixed when we chose the z as the quantization axis. To change the sign of the Chern number, we must change and revert the quantization axis. From this fact, we expect magnetic domain walls on CrI_3 to act effectively as topologically protected waveguides.

The starting Hamiltonian (1) displays complete time reversal symmetry. It is only after its spontaneous breaking that we can expect a non time reversal symmetry (TRS) Hamiltonian for the spin wave branch of excitations. It can be shown that performing TRS is equivalent to change the quantization axis from z to $-z$.

Replacing the Holstein-Primakoff transformation around the reversed axis leads to the complex conjugation of the coefficients of Eq. (4), followed by a $\mathbf{k} \to -\mathbf{k}$ transformation. The Hamiltonian (4) would be invariant under TRS if the coefficient β_a is real. When Kitaev's parameter K is turned on, we obtain $\mathcal{J}^{xy}_a \neq 0$. This makes β_a complex, so TRS is broken in our Hamiltonian. It is important to emphasize that the TRS breaking takes place through an anomalous A-B nearest-neighbor coupling in contrast to the normal A-A next-nearest-neighbor proposed by Refs. [22,31,32].

III. THERMAL HALL EFFECT

The magnon Hall effect corresponds to a transverse magnon-based heat current in response to a thermal gradient. First discovered in the ferromagnetic insulator $Lu_2V_2O_7$ [33], its explanation is understood in terms of magnon Berry's phases [34–38]. The intrinsic contribution associated with the transverse thermal conductivity is written in terms of the Berry curvature as follows [36]:

$$\kappa^{xy} = -\frac{k_B^2 T}{(2\pi)^2\hbar}\sum_n \int_{BZ} d^2k\, c_2(\rho_n)\mathbf{\Omega}^n_{\mathbf{k}}, \tag{11}$$

with $\rho_n = n_B(\epsilon_n(\mathbf{k}))$, n_B being the Bose distribution function, and

$$c_2(x) = (1+x)\ln^2\left(\frac{1+x}{x}\right) - \ln^2 x - 2\mathrm{Li}_2(-x), \tag{12}$$

where $\mathrm{Li}_s(x)$ is the polylogarithm of order s and argument x. In Fig. 3, we show the result for different values of K. We note

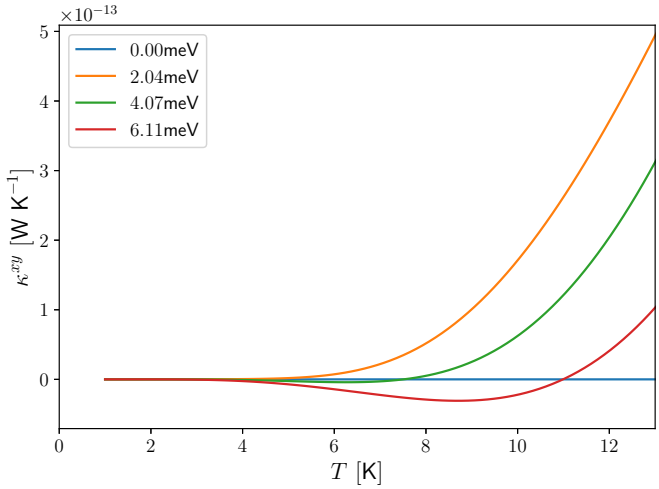

FIG. 3. Thermal Hall conductivity κ^{xy} vs temperature T. It can be seen that the conductivity changes of sign at different temperatures for different values of K. We highlight that for $K = 4.07$ meV, the thermal conductivity changes of sign for $T = 7.50$ K, which is highlighted by the grey dotted line.

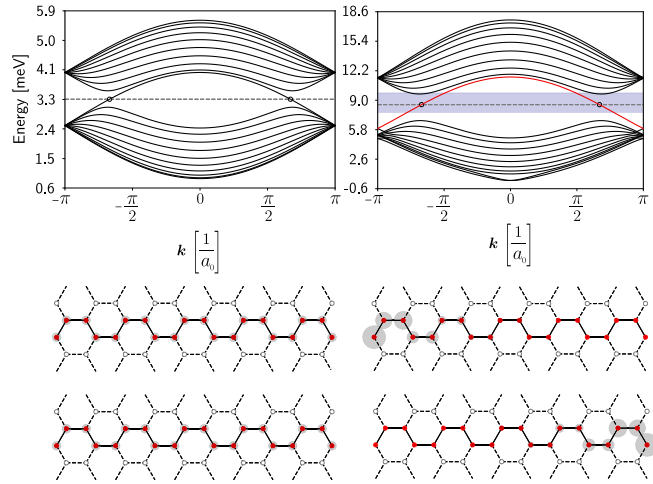

FIG. 4. Magnonic energy bands with $N = 10$ unit cells zigzag nanoribbon. (Left) Situation with $K = 0$. We can see a clear resemblance with those of graphene nanoribbons [43]. The otherwise flat bands in the mid-gap area are distorted due to the on-site energy discrepancy at the edge. The plots below represent the magnitude of the probabilities (grey circles with increasing radius for larger probabilities) for the states with $E = 3.25$ meV. There is no localization in this case. (Right) Situation with $K = 4.07$ meV. The bulk bands preserve their basic shape but the band-width is amplified. The degeneracy of the mid-gap bands, highlighted with red, toward the edge of the Brillouin zone gets lifted. The lower panels describe the probability density of the states with $E = 8.53$ meV. We can see clear evidence of the localization of these states at the geometrical edges of the ribbons.

that, for $K = 0$, there is no intrinsic contribution to magnon Hall effect. On the other hand, $K \neq 0$ leads to a nonvanishing contribution. We highlight the change in sign that the thermal Hall conductivity undergoes that has already been reported to occur in other materials [39,40]. Due to the monotonically decreasing behavior of c_2, the lower band will dominate the sign of the conductivity. At low temperatures, the function c_2 is relevant only in the vicinity of the $\mathbf{\Gamma}$ point, while at higher temperatures it acquires a contribution from the $\mathbf{K}$'s points, where the Berry curvature has the opposite sign, thus explaining the change of sign in the conductivity.

IV. NANORIBBONS

We now proceed to study the edge states in nanoribbons. This issue has been addressed extensively for magnon topological insulators based, for example, upon the Dzyalonshinskii-Moriya interaction in skyrmion crystals [23] and kagome lattices [41]. Recently it has been proposed to use edge states to implement topological magnon amplification [42].

We will study numerically the zigzag and armchair nanoribbons. For this, we must note that because only one direction is finite, the basis used to describe the material must change so that it includes the m distinguishable sites that form the nanoribbon. This can be captured in a general way by rewriting the original Hamiltonian as

$$H = -\frac{1}{2}\sum_{ii'jj'} S_{ij}^{\alpha}\mathcal{J}_{\boldsymbol{R}_i-\boldsymbol{R}_{i'}}^{jj'\alpha\beta}S_{i'j'}^{\alpha\beta} - \frac{1}{2}\sum_{ij} A_j\left(S_{ij}^{z}\right)^2, \tag{13}$$

where the indices $i, i' \in \{1, 2, \ldots N\}$ represent every unit cell, while the indices $j, j' \in \{1, 2, \ldots m\}$ correspond to every site inside each unit cell. Performing Holstein-Primakoff's transformation up to second order and Bloch's theorem on Hamiltonian (13), it is straightforward to prove that the magnonic Hamiltonian in $\boldsymbol{k}$ space is given by

$$\begin{aligned} H = -\frac{S}{4}\sum_{\boldsymbol{k}jj'}\big[&\Gamma_{\boldsymbol{k}}^{jj'+}a_{kj}^{\dagger}a_{kj'} + \Gamma_{\boldsymbol{k}}^{jj'-}a_{kj}^{\dagger}a_{-kj'}^{\dagger} \\ &- \mathcal{J}_0^{jj'zz}(a_{kj}^{\dagger}a_{kj} + a_{kj'}^{\dagger}a_{kj'}) + \text{H.c.}\big] \\ &+ \sum_{\boldsymbol{k}j}\left(SA_j + \mu_B g B_j^z\right)a_{kj}^{\dagger}a_{kj}, \end{aligned} \tag{14}$$

where

$$\Gamma_{\boldsymbol{k}}^{jj'\pm} = \mathcal{J}_{\boldsymbol{k}}^{jj'xx} \mp i\mathcal{J}_{\boldsymbol{k}}^{jj'xy} + i\mathcal{J}_{\boldsymbol{k}}^{jj'yx} \pm \mathcal{J}_{\boldsymbol{k}}^{jj'yy}, \tag{15a}$$

$$\mathcal{J}_{\boldsymbol{k}}^{jj'\mu\nu} = \sum_{ii'}\mathcal{J}_{\boldsymbol{R}_i-\boldsymbol{R}_{i'}}^{jj'\mu\nu}e^{-i\boldsymbol{k}\cdot(\boldsymbol{R}_i-\boldsymbol{R}_{i'})}. \tag{15b}$$

The obtained Hamiltonian can be easily adjusted to a particular nanoribbon by taking into account the geometrical properties of the lattice when building the exchange coupling $\mathcal{J}_{\boldsymbol{R}_i-\boldsymbol{R}_{i'}}^{jj'\mu\nu}$, procedure that is detailed in Appendix B. With this, we built the Hamiltonian for the zigzag and armchair cases and diagonalized them with Colpa's algorithm [28], obtaining the results shown Figs. 4 and 5.

Despite the striking similarities between the magnon Hamiltonian in absence of the Kitaev term and the usual tight-binding model for graphene [43], there is a subtle difference that becomes relevant in the case of edges, vacancies and similar defects. The diagonal contributions arise from exchange and are, therefore, dependent of the number of neighbors of each site. In this way, the local energy of the sites at the edge

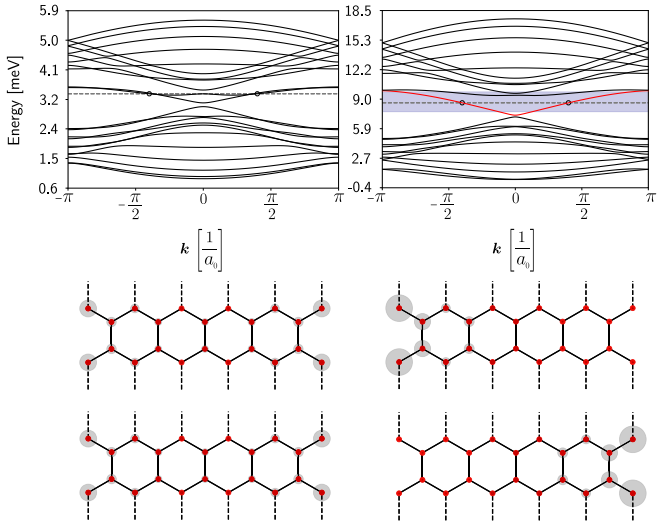

FIG. 5. Dispersion relation and states corresponding to the marked energies. (Left) Situation with $K = 0$. As with Fig. 4, there is a resemblance with graphene, where two of the top bands lower their energies due to the on-site energy discrepancy at the edge. The plots below represent the magnitude of the probabilities for the two possible states with $E = 3.23$ meV. The probability is proportional to the radii of the circles. (Right) Situation with $K = 4.07$ meV. Bands preserve their basic structure and the two central bands are separated. The light-blue colored area is the gap of the bulk, which shows which band should have a topological behavior. The lower plots represent the probability of the states with $E = 8.63$ meV. There is a clear localization at both edges of the ribbon.

is different from the ones in the bulk. As a result of the shift of the onsite energies at the edged, the flat band typically expected for zigzag ribbons [43] is now absent (see left panel of Fig. 4, where the ungapped dispersion in absence of the Kitaev term is displayed. More interestingly, when the Kitaev term is turned on, as in the right panel of Fig. 4, the bulk system acquired a gap which is bridged by the states marked in red. As shown in the lower panel, these states are localized around the sample's edges and are chiral.

V. CONCLUSIONS

In this paper, we have investigated the magnon spectrum of Heisenberg-Kitaev magnets, such as CrI_3. We have performed a spin wave analysis, based upon a Holstein-Primakoff representation around the out-of-plane preferred direction. We have found that the Kitaev term propagates the time-reversal symmetry breaking into the magnon sector. This is done through an anomalous nearest-neighbor contribution. That, in turn, leads to topological effects such as a gap in the Dirac point and edge states moving freely along domain walls and edges of the system. We expect that these discoveries will provide a handy tool for magnon based technologies. For example, the topologically protected states propagating at its edges or along domain walls can be used as an efficient method of magnon communication. Additionally the topological states can display the thermal Hall effect as shown in Refs. [34,36–38]. By comparing our results with the all-electron calculations of Ref. [30], we were able to provide early estimates of the magnetic constants of CrI_3.

ACKNOWLEDGMENTS

A.S.N. thanks Joaquin Fernández-Rossier for helpful comments. The authors thank Fondecyt Regular 1190324, N. V.-S. thanks Fondecyt Postdoctorado No. 3190264. A.S.N., R.J.-U., and E.A. thank Financiamiento Basal para Centros Científicos y Tecnológicos de Excelencia, Grant No. AFB180001, CEDENNA. L.E.F.F.T. acknowledges the support from the Abdus Salam International Center for Theoretical Physics through the Simons Foundation.

APPENDIX A: ANALYTICAL EXPRESSION FOR THE EIGENVALUES

Magnetic degrees of freedom in a CrI_3 monolayer can be modeled using the following Hamiltonian:

$$H = -\sum_{\langle i,j\rangle}\left(J\boldsymbol{S}_i\cdot\boldsymbol{S}_j + KS_i^{\gamma}S_j^{\gamma}\right) - \sum_i A\left(S_i^z\right)^2. \tag{A1}$$

To obtain the magnonic Hamiltonian, we perform Holstein-Primakoff's transformation by replacing $S_{i\mu}^{(x)} = \sqrt{\frac{S}{2}}(\psi_{i\mu}^{\dagger} + \psi_{i\mu})$, $S_{i\mu}^{(y)} = i\sqrt{\frac{S}{2}}(\psi_{i\mu}^{\dagger} - \psi_{i\mu})$, and $S_{i\mu}^{(z)} = S - \psi_{i\mu}^{\dagger}\psi_{i\mu}$, where $\mu \in \{A, B\}$ indexes the two lattices conforming the bipartite honeycomb array of Cr atoms. Then we define

$$\boldsymbol{\Psi}_{\boldsymbol{k}} = \begin{pmatrix} \psi_{A\boldsymbol{k}} \\ \psi_{B\boldsymbol{k}} \\ \psi_{A-\boldsymbol{k}}^{\dagger} \\ \psi_{B-\boldsymbol{k}}^{\dagger} \end{pmatrix} \tag{A2}$$

and keep terms up to quadratic order in $\boldsymbol{\Psi}_{\boldsymbol{k}}$. Hamiltonian can be expressed as a quadratic form $\mathcal{H} = \frac{1}{2}\sum_{\boldsymbol{k}} \boldsymbol{\Psi}_{\boldsymbol{k}}{}^{\dagger} H_{\boldsymbol{k}} \boldsymbol{\Psi}_{\boldsymbol{k}}$, where we have that

$$H_{\boldsymbol{k}} = \begin{pmatrix} \varepsilon & \alpha_{\boldsymbol{k}} & 0 & \beta_{\boldsymbol{k}} \\ \alpha_{\boldsymbol{k}}^{*} & \varepsilon & \beta_{-\boldsymbol{k}} & 0 \\ 0 & \beta_{-\boldsymbol{k}}^{*} & \varepsilon & \alpha_{\boldsymbol{k}} \\ \beta_{\boldsymbol{k}}^{*} & 0 & \alpha_{\boldsymbol{k}}^{*} & \varepsilon \end{pmatrix}. \tag{A3}$$

In the above expression, we have defined $\varepsilon = S(3J + K + 2A)$, $\alpha_{\boldsymbol{k}} = \sum_a \alpha_a e^{i\boldsymbol{k}\cdot\boldsymbol{\delta}_a}$, and $\beta_{\boldsymbol{k}} = \sum_a \beta_a e^{i\boldsymbol{k}\cdot\boldsymbol{\delta}_a}$, where we have defined the following quantities: $\alpha_a = -S(\mathcal{J}_a^{xx} + \mathcal{J}_a^{yy})/2$, $\beta_a = -S(\mathcal{J}_a^{xx} - \mathcal{J}_a^{yy})/2 - iS\mathcal{J}_a^{xy}$.

We perform a Bogoulivov transformation to the quadratic form, to find the allowed energies. In terms of $\epsilon_0 = S(3J + K)$, $\mathcal{K} = KS/\epsilon_0$ and $\mathcal{A} = 2AS/\epsilon_0$, the eigenvalues are found to be

$$\epsilon_{\pm}^2(\boldsymbol{k}) = \frac{\epsilon_0^2}{9}(f(\boldsymbol{k}) \pm \sqrt{g(\boldsymbol{k})}), \tag{A4}$$

with $\epsilon = 3JS + KS$ fixing the energy scale. Here we have defined functions $f(\boldsymbol{k}) = f_0(\boldsymbol{k}) + f_{\mathcal{A}}(\boldsymbol{k}) + f_{\mathcal{K}}(\boldsymbol{k})$ and $g(\boldsymbol{k}) = g_0(\boldsymbol{k}) + g_{\mathcal{A}}(\boldsymbol{k}) + g_{\mathcal{K}}(\boldsymbol{k})$, in such a way functions $f_{\mathcal{A},\mathcal{K}}(\boldsymbol{k})$ and $g_{\mathcal{A},\mathcal{K}}(\boldsymbol{k})$ were zero when $\mathcal{A}, \mathcal{K} = 0$, respectively. The functions $f(\boldsymbol{k})$ are defined as follows:

$$f_0(\boldsymbol{k}) = 2\left(2\cos\left(\frac{\sqrt{3}k_x a_0}{2}\right)\cos\left(\frac{k_y a_0}{2}\right) + \cos(k_y a_0) + 6\right), \tag{A5}$$

$$f_{\mathcal{A}}(\boldsymbol{k}) = 9\mathcal{A}(2 + \mathcal{A}), \tag{A6}$$

and

$$f_{\mathcal{K}}(\boldsymbol{k}) = \mathcal{K}^2\left(2\cos\left(\frac{\sqrt{3}k_x a_0}{2}\right)\cos\left(\frac{k_y a_0}{2}\right) + \cos(k_y a_0) - 3\right). \tag{A7}$$

While for functions $g(\boldsymbol{k})$, we have

$$g_0(\boldsymbol{k}) = 36\left(4\cos\left(\frac{\sqrt{3}k_x a_0}{2}\right)\cos\left(\frac{k_y a_0}{2}\right) + 2\cos(k_y a_0) + 3\right), \tag{A8}$$

$$g_{\mathcal{A}}(\boldsymbol{k}) = 36\mathcal{A}(\mathcal{A}+2)\left(4\cos\left(\frac{\sqrt{3}k_x a_0}{2}\right)\cos\left(\frac{k_y a_0}{2}\right) + 2\cos(k_y a_0) + 3\right), \tag{A9}$$

and

$$g_{\mathcal{K}}(\boldsymbol{k}) = \frac{3}{2}\mathcal{K}^2\Bigg[2\cos(\sqrt{3}k_x a_0)(\mathcal{K}^2 + 2 - (\mathcal{K}^2 - 4)\cos(k_y a_0)) - 2(\mathcal{K}^2+2)\left(8\cos\left(\frac{\sqrt{3}k_x a_0}{2}\right)\sin^2\left(\frac{k_y a_0}{2}\right)\cos\left(\frac{k_y a_0}{2}\right) + \cos(k_y a_0)\right) + (\mathcal{K}^2 - 4)(3 - \cos(2k_y a_0))\Bigg]. \tag{A10}$$

In the above definitions, $\mathcal{K}$ is a dimensionless parameter defined by

$$\mathcal{K} = \frac{K}{3J + K} \tag{A11}$$

which is bounded between $0 < \mathcal{K} < 1$, when $J, K > 0$. In this sense, $\mathcal{K}$ represents the relative strength of the Kitaev constant. Similarly, $\mathcal{A}$ is defined as

$$\mathcal{A} = \frac{2A}{3J + K} \tag{A12}$$

and it represents the relative magnitude of the anisotropy constant.

APPENDIX B: EDGE STATES IN CrI_3 NANORIBBONS

Recalling from the main body, we want to build the Hamiltonian for the zigzag and armchair nanoribbons:

$$H = -\frac{S}{4}\sum_{jj'k}\left[\Gamma_{\boldsymbol{k}}^{jj'-}a_{kj}^{\dagger}a_{-kj'}^{\dagger} + \bar{\Gamma}_{\boldsymbol{k}}^{jj'-}a_{-kj}a_{kj'} + \Gamma_{\boldsymbol{k}}^{jj'+}a_{kj}^{\dagger}a_{kj'} + \bar{\Gamma}_{\boldsymbol{k}}^{jj'+}a_{-kj}a_{-kj'}^{\dagger} - 2\mathcal{J}_0^{jj'zz}(a_{kj}^{\dagger}a_{kj} + a_{kj'}^{\dagger}a_{kj'})\right] + \sum_{jk}\left(SA_j + \mu_B g B_j^z\right)a_{kj}^{\dagger}a_{kj}, \tag{B1}$$

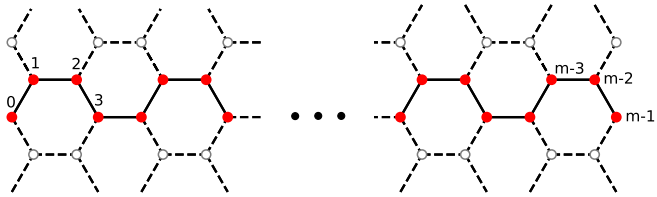

FIG. 6. Zigzag nanoribbon. The numbers beside the site correspond to the indices j and j' that are used in Hamiltonian (14).

where $j, j' \in \{0, 2, \ldots, m-1\}$ specify the site within the unit cell, and the coefficients $\Gamma_{\boldsymbol{k}}^{jj'\pm}$ and $\bar{\Gamma}_{\boldsymbol{k}}^{jj'\pm}$ are given by the fourier transform of the anisotropic exchange $\mathcal{J}_{\boldsymbol{k}}^{jj'\mu\nu} = \sum_{ii'}\mathcal{J}_{\boldsymbol{R}_i-\boldsymbol{R}_{i'}}^{jj'\mu\nu}e^{-i\boldsymbol{k}\cdot(\boldsymbol{R}_i-\boldsymbol{R}_{i'})}$ between sites j and j':

$$\Gamma_{\boldsymbol{k}}^{jj'\pm} = \mathcal{J}_{\boldsymbol{k}}^{jj'xx} \mp i\mathcal{J}_{\boldsymbol{k}}^{jj'xy} + i\mathcal{J}_{\boldsymbol{k}}^{jj'yx} \pm \mathcal{J}_{\boldsymbol{k}}^{jj'yy}, \tag{B2a}$$

$$\bar{\Gamma}_{i-i'}^{jj'\pm} = \mathcal{J}_{\boldsymbol{k}}^{jj'xx} \pm i\mathcal{J}_{\boldsymbol{k}}^{jj'xy} - i\mathcal{J}_{\boldsymbol{k}}^{jj'yx} \pm \mathcal{J}_{\boldsymbol{k}}^{jj'yy}. \tag{B2b}$$

As mentioned in the main body, in order to diagonalize Hamiltonian (B1) we must identify the shape of $\mathcal{J}_{\boldsymbol{k}}^{jj'\mu\nu}$ for the zigzag and armchair nanoribbons. For the former, we will consider that j and j' are numbered as shown in Fig. 6. From this figure, we can note that the lattice vector is $\boldsymbol{b} = (0, a_0, 0)$. This implies that the anisotropic exchange for the zigzag

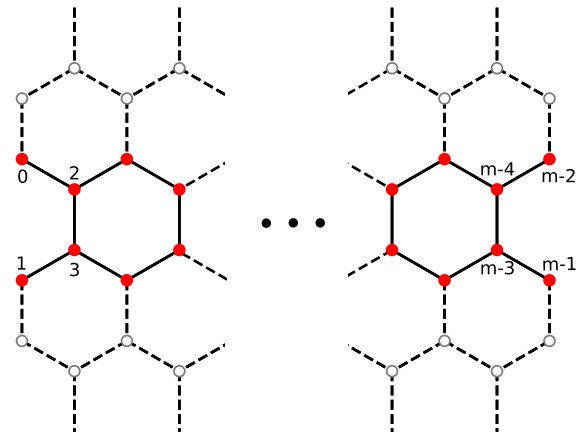

FIG. 7. Armchair nanoribbon. The numbers beside the site correspond to the indices j and j' that are used in Hamiltonian (14).

nanoribbon is given by

$$\mathcal{J}_{\boldsymbol{k}}^{jj'\mu\nu} = \begin{cases} \mathcal{J}_1^{\mu\nu}\delta_{j,j'+1} + \mathcal{J}_2^{\mu\nu}e^{i\boldsymbol{k}\cdot\boldsymbol{b}}\delta_{j,j'-1} + \mathcal{J}_3^{\mu\nu}\delta_{j,j'-1} & \text{if } j = 4n \\ \mathcal{J}_1^{\mu\nu}\delta_{j,j'-1} + \mathcal{J}_2^{\mu\nu}e^{-i\boldsymbol{k}\cdot\boldsymbol{b}}\delta_{j,j'+1} + \mathcal{J}_3^{\mu\nu}\delta_{j,j'+1} & \text{if } j = 4n+1 \\ \mathcal{J}_1^{\mu\nu}\delta_{j,j'+1} + \mathcal{J}_2^{\mu\nu}\delta_{j,j'-1} + \mathcal{J}_3^{\mu\nu}e^{-i\boldsymbol{k}\cdot\boldsymbol{b}}\delta_{j,j'-1} & \text{if } j = 4n+2 \\ \mathcal{J}_1^{\mu\nu}\delta_{j,j'-1} + \mathcal{J}_2^{\mu\nu}\delta_{j,j'+1} + \mathcal{J}_3^{\mu\nu}e^{i\boldsymbol{k}\cdot\boldsymbol{b}}\delta_{j,j'+1} & \text{if } j = 4n+3 \end{cases} \tag{B3}$$

with $n \in \mathbb{Z}$.

In the case of the armchair nanoribbon, we will consider the unit cell of Fig. 7, where the lattice vector is given by $\boldsymbol{b} = (0, \sqrt{3}a_0, 0)$. With these considerations it is straightforward to obtain that the anisotropic exchange coupling reads

$$\mathcal{J}_{\boldsymbol{k}}^{jj'\mu\nu} = \begin{cases} \mathcal{J}_1^{\mu\nu}e^{i\boldsymbol{k}\cdot\boldsymbol{b}}\delta_{j,j'-1} + \mathcal{J}_2^{\mu\nu}\delta_{j,j'+2} + \mathcal{J}_3^{\mu\nu}\delta_{j,j'-2} & \text{if } j = 4n \\ \mathcal{J}_1^{\mu\nu}e^{-i\boldsymbol{k}\cdot\boldsymbol{b}}\delta_{j,j'+1} + \mathcal{J}_2^{\mu\nu}\delta_{j,j'-2} + \mathcal{J}_3^{\mu\nu}\delta_{j,j'+2} & \text{if } j = 4n+1 \\ \mathcal{J}_1^{\mu\nu}\delta_{j,j'-1} + \mathcal{J}_2^{\mu\nu}\delta_{j,j'-2} + \mathcal{J}_3^{\mu\nu}\delta_{j,j'+2} & \text{if } j = 4n+2 \\ \mathcal{J}_1^{\mu\nu}\delta_{j,j'+1} + \mathcal{J}_2^{\mu\nu}\delta_{j,j'+2} + \mathcal{J}_3^{\mu\nu}\delta_{j,j'-2} & \text{if } j = 4n+3 \end{cases}. \tag{B4}$$

[1] K. S. Novoselov, A. K. Geim, S. V. Morozov, D. Jiang, Y. Zhang, S. V. Dubonos, I. V. Grigorieva, and A. A. Firsov, Electric field effect in atomically thin carbon films, Science **306**, 666 (2004).

[2] K. S. Novoselov, A. Mishchenko, A. Carvalho, and A. H. C. Neto, 2D materials and van der Waals heterostructures, Science **353**, aac9439 (2016).

[3] A. Castellanos-Gomez, Why all the fuss about 2D semiconductors? Nat. Photon. **10**, 202 (2016).

[4] J. M. Lu, O. Zheliuk, I. Leermakers, N. F. Q. Yuan, U. Zeitler, K. T. Law, and J. T. Ye, Evidence for two-dimensional Ising superconductivity in gated MoS_2, Science **350**, 1353 (2015).

[5] M. M. Ugeda, A. J. Bradley, Y. Zhang, S. Onishi, Y. Chen, W. Ruan, C. Ojeda-Aristizabal, H. Ryu, M. T. Edmonds, H.-Z. Tsai, A. Riss, S.-K. Mo, D. Lee, A. Zettl, Z. Hussain, Z.-X. Shen, and M. F. Crommie, Characterization of collective ground states in single-layer $NbSe_2$, Nat. Phys. **12**, 92 (2016).

[6] K. Chang, J. Liu, H. Lin, N. Wang, K. Zhao, A. Zhang, F. Jin, Y. Zhong, X. Hu, W. Duan, Q. Zhang, L. Fu, Q.-K. Xue, X. Chen, and S.-H. Ji, Discovery of robust in-plane ferroelectricity in atomic-thick SnTe, Science **353**, 274 (2016).

[7] S. Roche, Johan Åkerman, B. Beschoten, J.-C. Charlier, M. Chshiev, S. P. Dash, B. Dlubak, J. Fabian, A. Fert, M. Guimarães, F. Guinea, I. Grigorieva, C. Schönenberger, P. Seneor, C. Stampfer, S. O. Valenzuela, X. Waintal, and B. v. Wees, Graphene spintronics: The European Flagship perspective, 2D Mater. **2**, 030202 (2015).

[8] L. A. Benítez, W. Savero Torres, J. F. Sierra, M. Timmermans, J. H. Garcia, S. Roche, M. V. Costache, and S. O. Valenzuela, Tunable room-temperature spin galvanic and spin Hall effects in van der Waals heterostructures, Nat. Mater. **19**, 170 (2020).

[9] B. Huang, G. Clark, E. Navarro-Moratalla, D. R. Klein, R. Cheng, K. L. Seyler, D. Zhong, E. Schmidgall, M. A. McGuire, D. H. Cobden, W. Yao, D. Xiao, P. Jarillo-Herrero, and X. Xu, Layer-dependent ferromagnetism in a van der Waals crystal down to the monolayer limit, Nature (London) **546**, 270 (2017).

[10] C. Gong, L. Li, Z. Li, H. Ji, A. Stern, Y. Xia, T. Cao, W. Bao, C. Wang, Y. Wang, Z. Q. Qiu, R. J. Cava, S. G. Louie, J. Xia, and X. Zhang, Discovery of intrinsic ferromagnetism in two-dimensional van der Waals crystals, Nature (London) **546**, 265 (2017).

[11] N. D. Mermin and H. Wagner, Absence of Ferromagnetism or Antiferromagnetism in One- or Two-Dimensional Isotropic Heisenberg Models, Phys. Rev. Lett. **17**, 1133 (1966).

[12] J. L. Lado and J. Fernández-Rossier, On the origin of magnetic anisotropy in two dimensional CrI_3, 2D Mater. **4**, 035002 (2017).

[13] A. Auerbach, *Interacting Electrons and Quantum Magnetism* (Springer-Verlag, New York, 1994).

[14] V. V. Kruglyak, S. O. Demokritov, and D. Grundler, Magnonics, J. Phys. D **43**, 260301 (2010).

[15] A. Chumak, V. Vasyuchka, A. Serga, and B. Hillebrands, Magnon spintronics, Nat. Phys. **11**, 453 (2015).

[16] I. Lee, F. G. Utermohlen, D. Weber, K. Hwang, C. Zhang, J. van Tol, J. E. Goldberger, N. Trivedi, and P. C. Hammel, Fundamental Spin Interactions Underlying the Magnetic Anisotropy in the Kitaev Ferromagnet CrI_3, Phys. Rev. Lett. **124**, 017201 (2020).

[17] C. Xu, J. Feng, H. Xiang, and L. Bellaiche, Interplay between kitaev interaction and single ion anisotropy in ferromagnetic CrI_3 and $CrGeTe_3$ monolayers, npj Comput. Mater. **4**, 57 (2018).

[18] G. Jackeli and G. Khaliullin, Mott Insulators in the Strong Spin-Orbit Coupling Limit: From Heisenberg to a Quantum Compass and Kitaev Models, Phys. Rev. Lett. **102**, 017205 (2009).

[19] A. Kitaev, Anyons in an exactly solved model and beyond, Ann. Phys. **321**, 2 (2006).

[20] M. Hermanns, I. Kimchi, and J. Knolle, Physics of the Kitaev model: Fractionalization, dynamic correlations, and material connections, Annu. Rev. Condens. Matter Phys. **9**, 17 (2018).

[21] R. Shindou, R. Matsumoto, S. Murakami, and J.-i. Ohe, Topological chiral magnonic edge mode in a magnonic crystal, Phys. Rev. B **87**, 174427 (2013).

[22] S. A. Owerre, A first theoretical realization of honeycomb topological magnon insulator, J. Phys.: Condens. Matter **28**, 386001 (2016).

[23] A. Roldán-Molina, A. S. Nunez, and J. Fernández-Rossier, Topological spin waves in the atomic-scale magnetic skyrmion crystal, New J. Phys. **18**, 045015 (2016).

[24] R. Hidalgo-Sacoto, R. I. Gonzalez, E. E. Vogel, S. Allende, J. D. Mella, C. Cardenas, R. E. Troncoso, and F. Munoz, Magnon valley Hall effect in CrI_3-based vdW heterostructures, Phys. Rev. B **101**, 205425 (2020).

[25] M. Gohlke, R. Verresen, R. Moessner, and F. Pollmann, Dynamics of the Kitaev-Heisenberg Model, Phys. Rev. Lett. **119**, 157203 (2017).

[26] D. G. Joshi, Topological excitations in the ferromagnetic Kitaev-Heisenberg model, Phys. Rev. B **98**, 060405(R) (2018).

[27] T. Holstein and H. Primakoff, Field dependence of the intrinsic domain magnetization of a ferromagnet, Phys. Rev. **58**, 1098 (1940).

[28] J. Colpa, Diagonalization of the quadratic boson hamiltonian, Physica A: Stat. Mech. Appl. **93**, 327 (1978).

[29] W. Jin, H. H. Kim, Z. Ye, S. Li, P. Rezaie, F. Diaz, S. Siddiq, E. Wauer, B. Yang, C. Li, S. Tian, K. Sun, H. Lei, A. W. Tsen, L. Zhao, and R. He, Raman fingerprint of two terahertz spin wave branches in a two-dimensional honeycomb Ising ferromagnet, Nat. Commun. **9**, 1 (2018).

[30] A. T. Costa, D. L. R. Santos, N. M. R. Peres, and J. Fernández-Rossier, Topological magnons in CrI_3 monolayers: an itinerant fermion description, arXiv:2002.00077 [cond-mat].

[31] L. Chen, J.-H. Chung, B. Gao, T. Chen, M. B. Stone, A. Kolesnikov, Q. Huang, and P. Dai, Topological Spin Excitations in Honeycomb Ferromagnet CrI_3, Phys. Rev. X **8**, 041028 (2018).

[32] S. K. Kim, H. Ochoa, R. Zarzuela, and Y. Tserkovnyak, Realization of the Haldane-Kane-Mele Model in a System of Localized Spins, Phys. Rev. Lett. **117**, 227201 (2016).

[33] Y. Onose, T. Ideue, H. Katsura, Y. Shiomi, N. Nagaosa, and Y. Tokura, Observation of the magnon Hall effect, Science **329**, 297 (2010).

[34] H. Katsura, N. Nagaosa, and P. A. Lee, Theory of the Thermal Hall Effect in Quantum Magnets, Phys. Rev. Lett. **104**, 066403 (2010).

[35] R. Matsumoto and S. Murakami, Theoretical Prediction of a Rotating Magnon Wave Packet in Ferromagnets, Phys. Rev. Lett. **106**, 197202 (2011).

[36] R. Matsumoto, R. Shindou, and S. Murakami, Thermal Hall effect of magnons in magnets with dipolar interaction, Phys. Rev. B **89**, 054420 (2014).

[37] A. Mook, J. Henk, and I. Mertig, Magnon Hall effect and topology in kagome lattices: A theoretical investigation, Phys. Rev. B **89**, 134409 (2014).

[38] T. Ideue, Y. Onose, H. Katsura, Y. Shiomi, S. Ishiwata, N. Nagaosa, and Y. Tokura, Effect of lattice geometry on magnon Hall effect in ferromagnetic insulators, Phys. Rev. B **85**, 134411 (2012).

[39] G. Grissonnanche, A. Legros, S. Badoux, E. Lefrancois, V. Zatko, M. Lizaire, F. Laliberte, A. Gourgout, J.-S. Zhou, S. Pyon *et al.*, Giant thermal Hall conductivity in the pseudogap phase of cuprate superconductors, Nature (London) **571**, 376 (2019).

[40] Y. Kasahara, K. Sugii, T. Ohnishi, M. Shimozawa, M. Yamashita, N. Kurita, H. Tanaka, J. Nasu, Y. Motome, T. Shibauchi *et al.*, Unusual Thermal Hall Effect in a Kitaev Spin Liquid Candidate α-$RuCl_3$, Phys. Rev. Lett. **120**, 217205 (2018).

[41] A. Mook, J. Henk, and I. Mertig, Edge states in topological magnon insulators, Phys. Rev. B **90**, 024412 (2014).

[42] D. Malz, J. Knolle, and A. Nunnenkamp, Topological magnon amplification, Nat. Commun. **10**, 3937 (2019).

[43] L. E. F. Foa Torres, S. Roche, and J.-C. Charlier, *Introduction to Graphene-Based Nanomaterials: From Electronic Structure to Quantum Transport*, 2nd ed. (Cambridge University Press, Cambridge, 2020).